Supplementary information

Tuning the structure and habit of iron oxide mesocrystals

Erik Wetterskog, [*ab] Alice Klapper,[c] Sabrina Disch,[d] Elisabeth Josten,[ce] Raphaël P. Hermann,[cf] Ulrich Rücker,[c] Thomas Brückel,[c] Lennart Bergström,[a] and German Salazar-Alvarez[*a]

[a.] *Department of Materials and Environmental Chemistry, Arrhenius Laboratory, Stockholm University, Sweden*

[b.] *Department of Engineering Sciences, Ångström Laboratory, Uppsala University, Sweden*

[c.] *Jülich Centre for Neutron Science JCNS and Peter Grünberg Institut PGI, JARA-FIT, Forschungszentrum Jülich, 52425 Jülich, Germany*

[d.] *Department of Chemistry, Universität zu Köln, 50939 Köln, Germany.*

[e.] *Helmholtz-Zentrum Dresden-Rossendorf, Institute of Ion Beam Physics and Materials Research, Bautzner Landstr. 400, 01328 Dresden, Germany*

[f.] *Materials Science and Technology Division, Oak Ridge National Laboratory, Oak Ridge, 37831 Tennessee, USA*

ADDITIONAL CHARACTERIZATION OF THE IRON OXIDE NANOCUBES AND MESOCRYSTALS

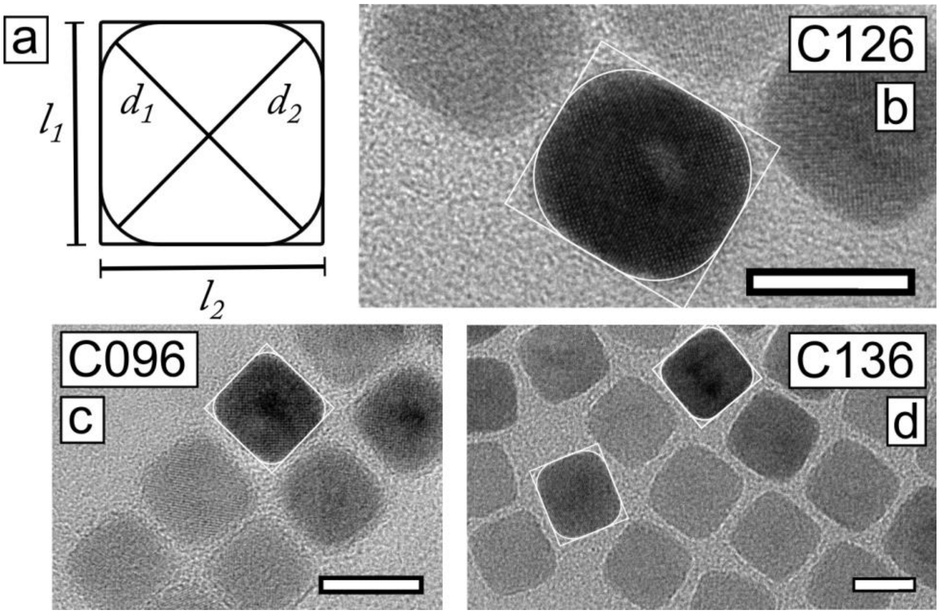

Figure S 1: Illustration of the method used to estimate the superellipse exponent *n*. (a) Schematic representation of the measured distances and (b-d) examples of TEM images of contour-traced nanocubes with different sizes. Scale bar represents 10 nm.

Transmission electron microscopy. High-resolution bright field-TEM images were acquired using a JEOL JEM-2100 microscope (Filament: LaB_6 200 kV, C_s =1.4 mm, C_c =1.8 mm, point resolution = 2.5 Å, line resolution = 1.4 Å) equipped with a GATAN SC1000 Orius camera for high resolution imaging. Further information regarding the preparation and characterization (particle size determination, TEM images, powder X-ray diffraction) of the nanocube samples C086, C096, C126 and C136 are given in refs [1,2].[1,2]

Determination of nanocube shape. Details on the characterization of the particle shape with a superellipse approximation: $x^n + y^n = \left(\frac{l}{2}\right)^n$ are as follows: a rectangle covering the particle is drawn by hand using a ruler with a right angle. The corner (*i.e.* the contour) of the rounded cube is traced by hand. The edge lengths l_1 and l_2 and the diagonals d_1 and d_2 are measured for 30-40 nanocubes for each sample. The parameter n can then be found through:

$$n = \frac{-\ln 2}{\ln d - \ln \sqrt{l_1^2 + l_2^2}}$$

The volume of a nanoparticle V_p can be estimated assuming a superellipsoid. For a superellipsoid expressed as $x^n + y^n + z^n = \left(\frac{l}{2}\right)^n$ with exponent n, the volume is given by:

$$V_p = l^3 \frac{\left[\Gamma\left(1 + \frac{1}{n}\right)\right]^3}{\Gamma\left(1 + \frac{3}{n}\right)}$$

where Γ is the gamma function.

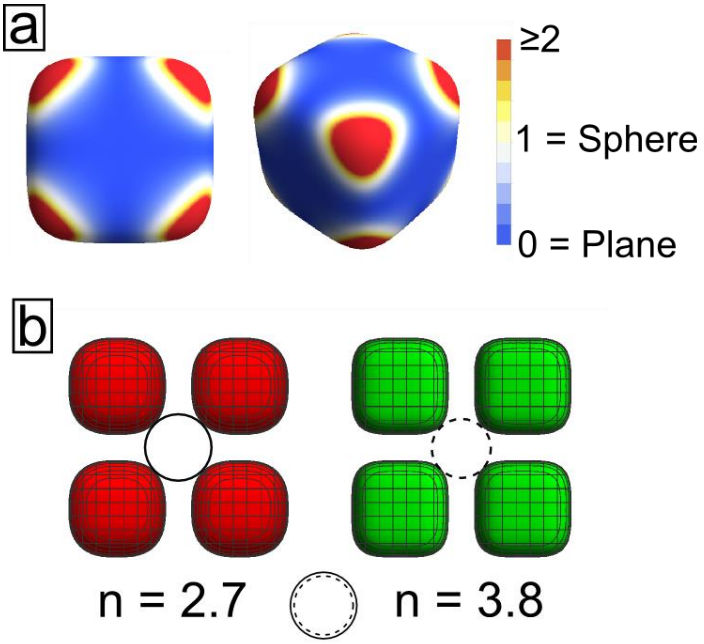

Figure S 2: Gaussian curvature of a superellipsoid and illustration of the hole size in a p4mm layer of superellipsoids. (a) Gaussian curvature (K) of a superellipsoid with equal semi-axes a = 1 and n = 4. The maximum Gaussian curvature for this particular superellipsoid is K ~ 6 (at the corners), but the scale is capped at K = 2 for clarity. Colors hotter than white in the temperature scale represents part of the surface with a higher curvature than a sphere of equal radius (K = 1). (b) 2D illustration of the holes in the layers of the *bct* lattice. A comparative illustration of the hole size for two equal lattices based on different superellipsoids is shown.

GISAXS

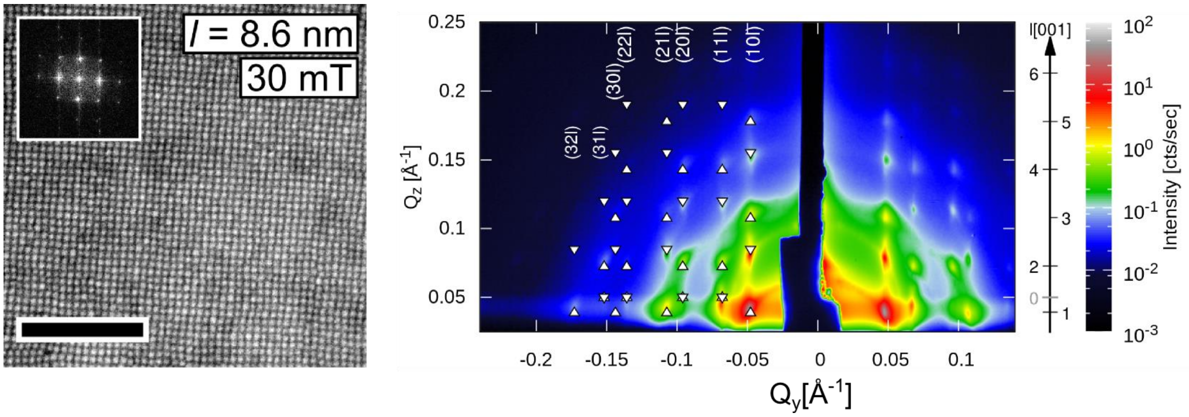

Figure S 3: HRSEM image and GISAXS pattern of an array of nanocubes C086 assembled in a vertical magnetic field of strength *μ_0H* = 30 mT. Indexing refers to a *bct* lattice in the [001]-orientation. See reference [2] for a further description on this system.[2] Scale bar: 100 nm.

Indexing of the [101] oriented *bct* lattice

In order to be able to distinguish the in-plane and out-of-plane symmetries in the GISAXS pattern, the $[101]_{MC}$ orientation of the *bct* lattice is indexed as an orthorhombic lattice with $c \perp$ the substrate (see Fig. S4. The orthorhombic lattice parameters are derived by transformation of the *bct* lattice into this lower symmetry lattice, for an ideal ratio of $c_t/a_t = \sqrt{3}$ according to

$$\overrightarrow{a_o} = a_t$$

$$\overrightarrow{b_o} = \overrightarrow{b_t} + \overrightarrow{c_t}$$

$$\overrightarrow{c_o} = \overrightarrow{c_t} - 3\,\overrightarrow{b_t}$$

where the subscripts o and t denote the orthorhombic and tetragonal lattices, respectively. Using the tetragonal symmetry conditions $a_t = b_t$ and α = β = γ = 90° along with the ideal ratio of $c_t/a_t = \sqrt{3}$ we obtain for the orthorhombic lattice parameters:

$$a_o = a_t$$

$$b_o = 2a_t$$

$$c_o = \sqrt{12}a_t$$

Indeed, the orthorhombic lattice parameters determined by GISAXS (Table S1) are in excellent agreement with these geometric relations, confirming (along with the observed systematic reflection extinctions) the proposed mesocrystal structure orientation. However, slight deviations from these ideal lattice parameters may occur related to distortions of the lattice and, in particular, a vertical contraction of the entire mesocrystals that is often observed upon final drying. Such a vertical contraction makes exact comparisons between the lattice parameters of the standard *bct* lattice and the rotated *bct* lattice slightly imprecise. Small distortions result in slight deviations from the tetragonal symmetry conditions: $a = b$ and α = β = γ = 90°. The lattice parameters (a_r, b_r, c_r) of the rotated *bct* cell are shown in Figure 2b. Nonetheless we find that the lattice parameter b_r (which is not parallel to the surface) is just slightly shorter with respect to a_r (0.03-3%). These small contractions are likely an effect of a previously reported drying mechanism.[3]

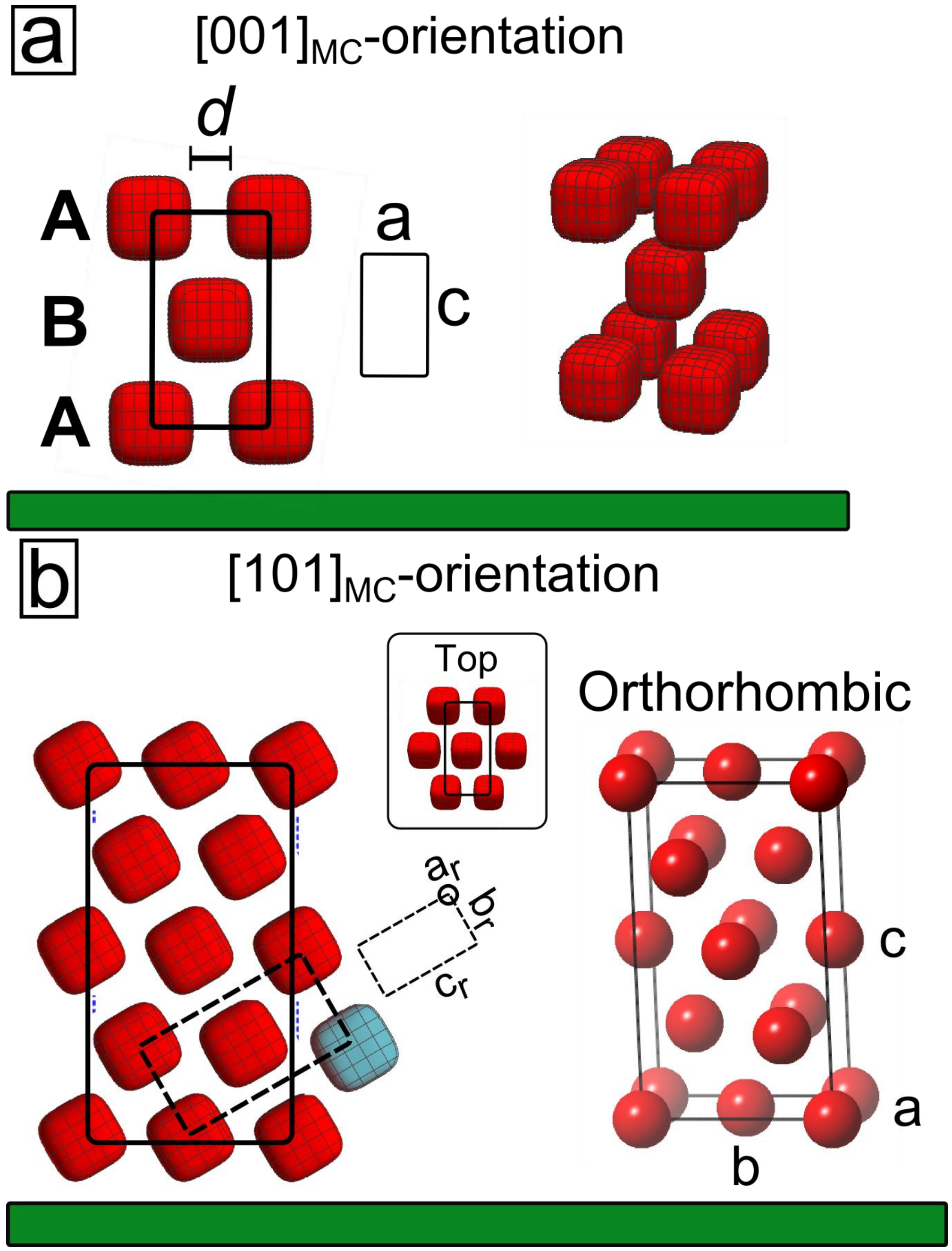

Figure S 4: An additional illustration of the two structures presented in the main manuscript. (a) Representation of the $[001]_{MC}$-oriented *bct* structure, and (b) the $[101]_{MC}$ oriented *bct* lattice and its relation to the orthorhombic unit cell (b) used to index the GISAXS data. The axes shown in the diagram are the axes used in Table S1.

Table S 1: Lattice parameters derived from GISAXS analysis. The "rotated *bct*" parameters are derived from the orthorhombic lattice parameters.

Standard *bct* – body centered tetragonal (Simple cubic – sc, in case of C136)						
Array	*a* (nm)	Error *a* (nm)	*b* (nm)	Error *b* (nm)	*c* (nm)	Error *c* (nm)
C086	13.10	0.05	= *a*		17.8	0.05
C096	13.70	0.13			23.35	0.25
C126	16.01	0.14			26.8	0.2
C136	17.10	0.16			Same as *a*	
Orthorhombic						
C096	13.69	0.24	26.75	0.19	47.6	0.6
C126	15.75	0.33	30.92	0.27	53.75	0.25
C136	17.31	0.42	34.19	0.12	57.6	0.9
Rotated *bct* – distorted body centered tetragonal						
C096	13.69	0.24	≈ *a*		23.33	0.21
C126	15.75	0.33			26.80	0.16
C136	17.31	0.42			29.4	0.28

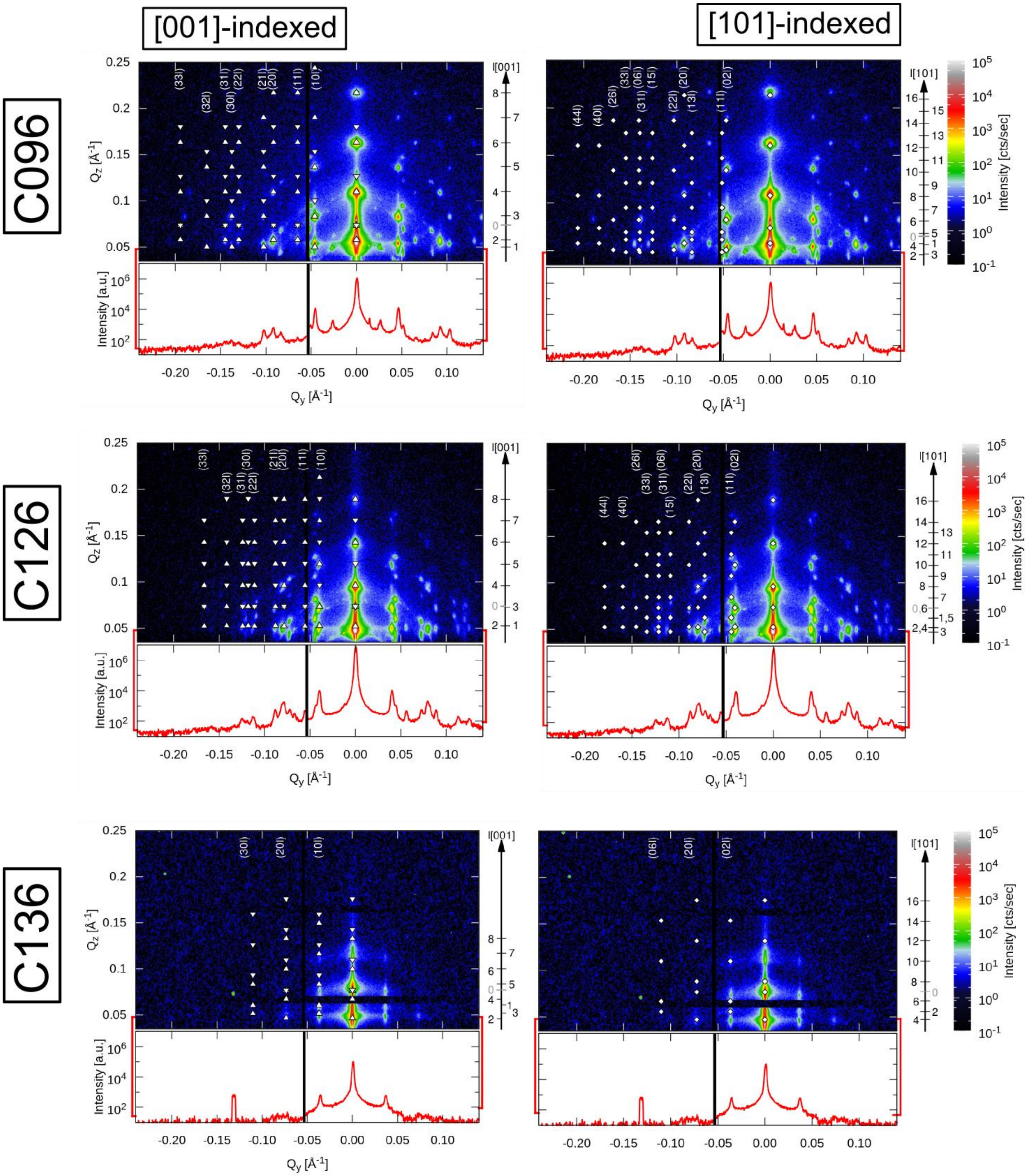

Figure S 5: GISAXS patterns of the dried-out mesocrystals assembled in zero-field showing the indexing of the $[001]_{MC}$ and the $[101]_{MC}$ growth orientation. Indexing of (a) [001]-oriented *bct* structure (in case of the C136 the pattern is indexed to a *sc* lattice). (b) Indexing of the orthorhombic lattice shown in Figure S4b, corresponding to an [101]-oriented *bct* lattice.

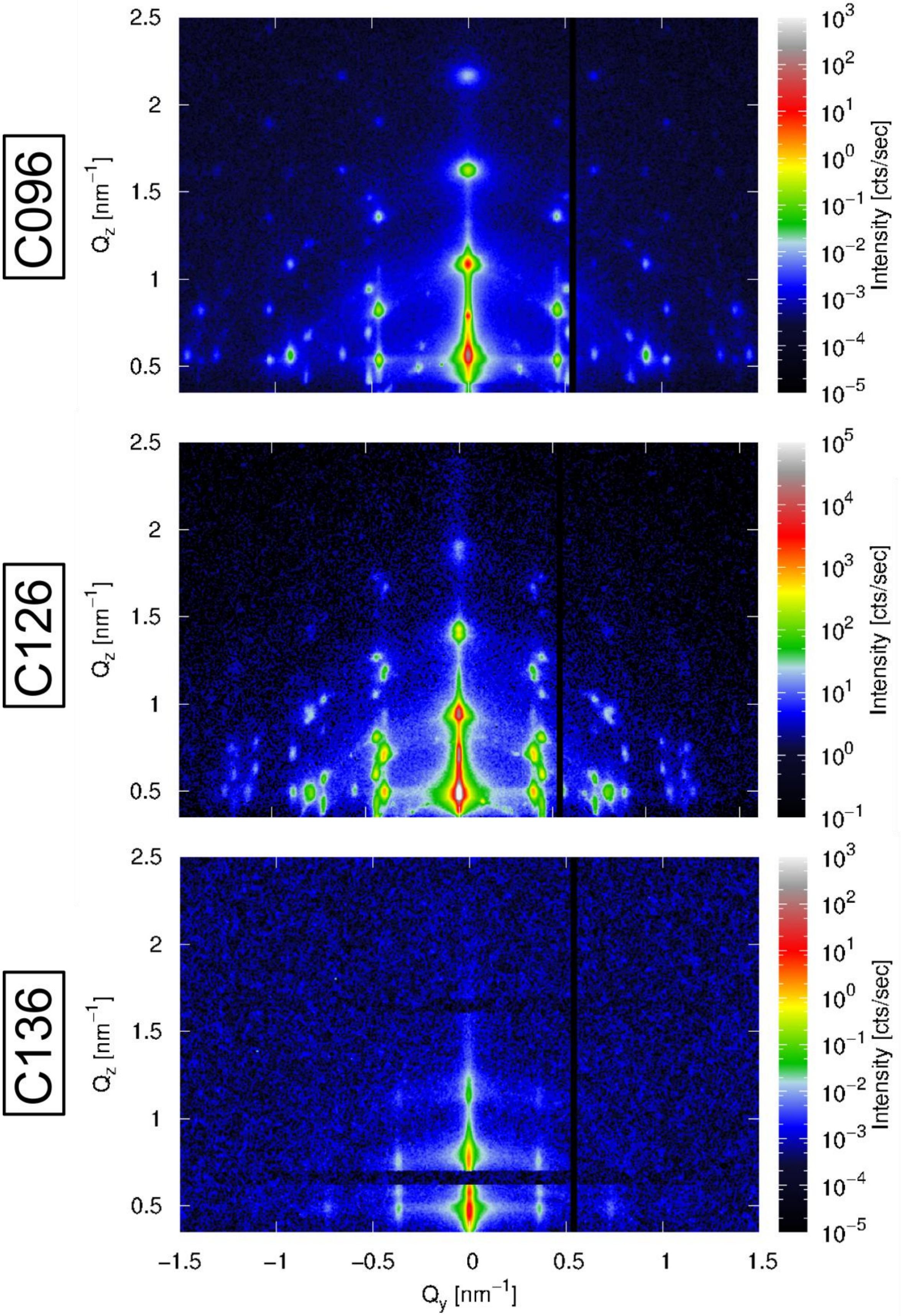

Figure S 6: GISAXS patterns of the dried-out mesocrystals assembled in zero-field (no indexes).

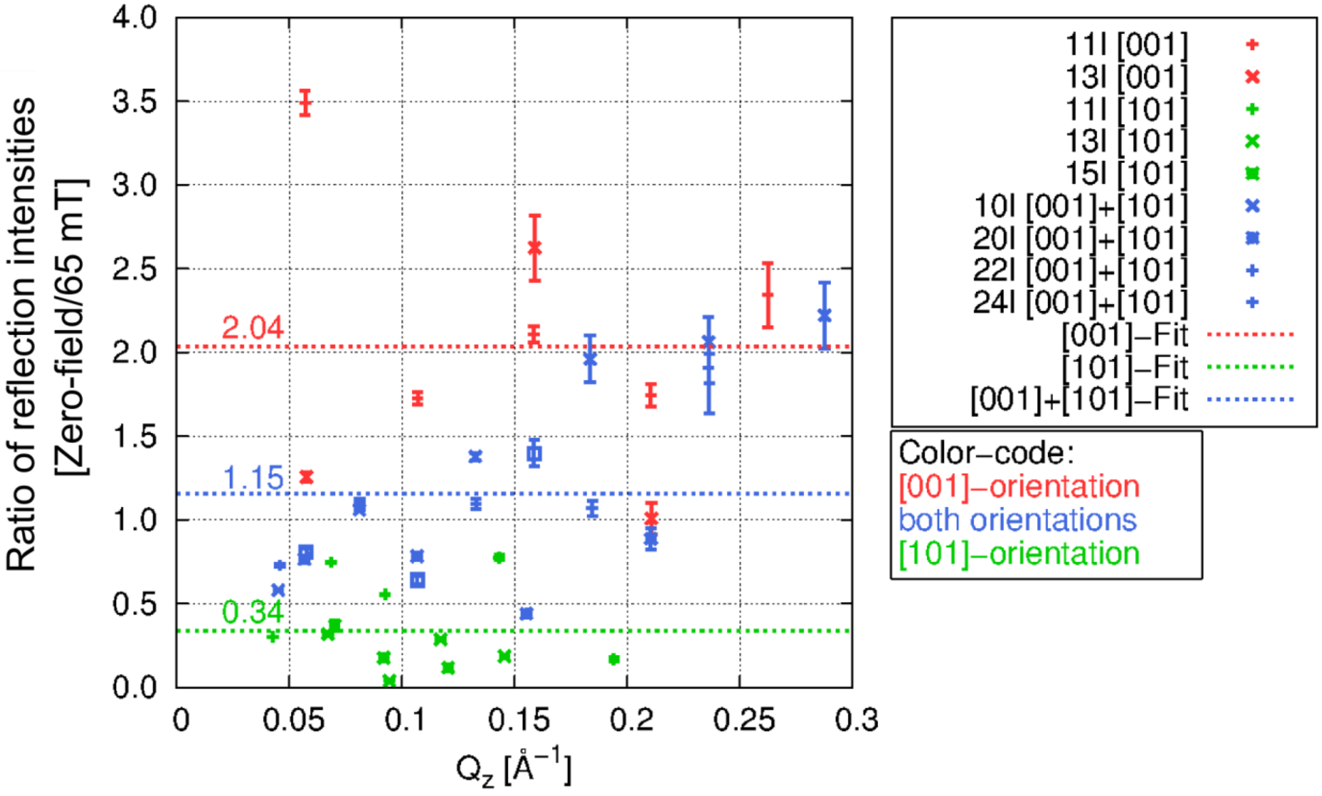

Figure S 7: Analysis of the ratio of the reflection intensities of the C096 mesocrystals. A plot of the ration reflection intensities plotted *vs.* scattering vector. The different colors correspond to $[001]_{MC}$ (red), $[001]_{MC}$ + $[101]_{MC}$ (blue), and $[101]_{MC}$ (green).

In order to estimate the preferred orientation of the *bct* lattice after deposition in applied field and in zero field, the relative scattering intensities observed in the respective GISAXS patterns are analyzed. However, in order to avoid systematic errors due to *Q* dependent features such as the spatial variation of the nanoparticle form factor and refractive scattering contributions, only the scattering intensities observed at the same *Q* position can be compared directly. We thus determined the relative intensities of GISAXS reflections in mesocrystal samples assembled in zero field and upon application of a weak magnetic field as follows:

$$\frac{[001]_{ZF}}{[001]_{F}} = A$$

$$\frac{[101]_{ZF}}{[101]_{F}} = B$$

$$\frac{([001] + [101])_{ZF}}{([001] + [101])_{F}} = C$$

where A and B are the relative intensity ratios of reflections that are uniquely associated with the [001] and [101] orientation of the *bct* lattice, respectively. C denotes the intensity ratio of reflections that are common to both orientations and is thus associated with instrumental parameters such as a different exposure time or amount of mesocrystals in the footprint of the X-ray beam in both measurements. These relative intensities displayed in Figure S7 already qualitatively suggest that the [001] orientation is preferred in zero field for the C096 nanocubes, whereas it is preferred in applied field for the C126 nanocubes. In order to obtain quantitative information on the preference of the lattice orientations, the above system of equations is solved, leading to

$$\frac{[001]_F}{[101]_F} = \frac{(B-C)}{(C-A)}$$

$$\frac{[001]_{ZF}}{[101]_{ZF}} = \frac{A(B-C)}{B(C-A)}$$

Using the intensity ratios: A, B, C determined above, we obtain a preference of [001] over [101] orientation of 1.02±0.53 and 6.14±4.52 in applied field and zero field, respectively, for C096 and 3.4±2.8 and 0.94±0.77 in applied field and zero field, respectively, for C126. Despite the large uncertainties, these results indicate that the [001] and [101] orientations are roughly equally preferred in zero field for C096 and in applied field for C126, whereas the [101] orientation is clearly preferred in applied field for C096 and in zero field for C126.

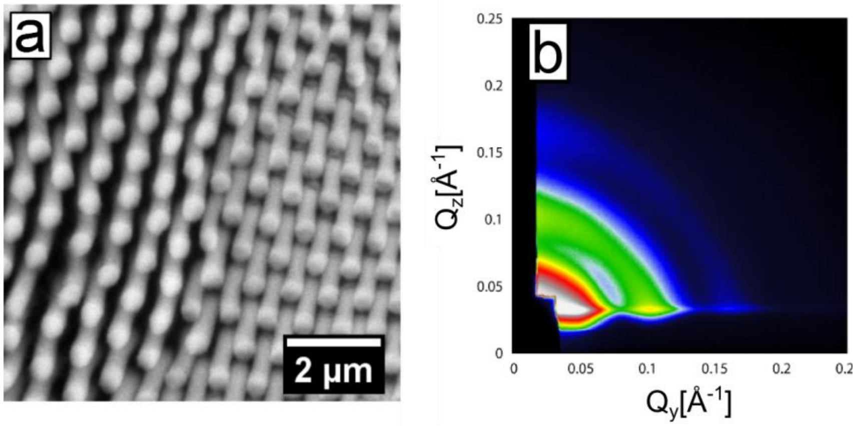

Figure S 8: (a) SEM image and (b) GISAXS pattern of the C086 pillars assembled in a magnetic field of $\mu_0 H$ = 200 mT.

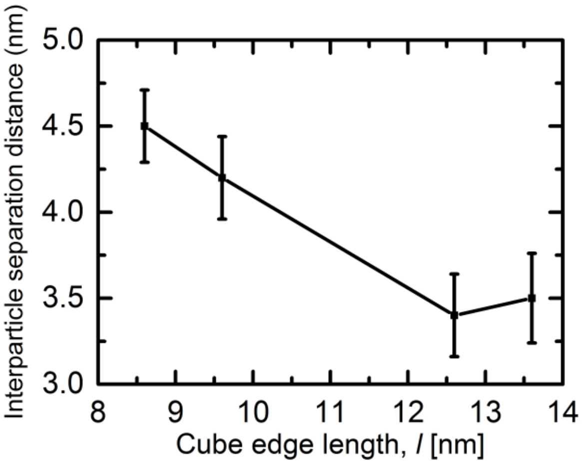

Figure S 9: Face-to-face separation distances ($d_0 = a - l$) between nanocubes in the basal plane of the *bct* structure.

The surface to surface interparticle distance $d_0 = a - l$ was calculated using the values obtained from table S1 and the edge lengths determined from TEM. The errors bars represent $\boldsymbol{\partial d_0} = \sqrt{(\boldsymbol{\partial a})^2 + (\boldsymbol{\partial l})^2}$. The error in the lattice parameter is given in Table S1 whereas the uncertainty of the edge length determination, $\boldsymbol{\partial l}$, was estimated to be ± 0.2 nm.

Table S 2: Calculated nanocube volume and particle volume fraction of the $[001]_{MC}$- and $[101]_{MC}$-structure. The uncertainty of the edge length determination, $\boldsymbol{\partial l}$, was as above estimated to be ± 0.2 nm. An uncertainty for the determination of the superellipsoid exponent of ± 0.2 was used to estimate the error of the superellipsoid volume. The errors of the mesocrystal lattice parameter determination are given in Table S1. Note that the estimated errors of the volume fraction are almost entirely due to errors with respect to the nanocube volume.

NC ID	NC Volume [nm^3]	Est. error [nm^3]	Volume fraction [001]	Est. error	Volume fraction [101]	Est error.
C086	430	30	0.28	0.02		
C096	700	50	0.32	0.02	0.32	0.02
C126	1400	80	0.41	0.03	0.43	0.02
C136	1980	100	0.40*	0.02	0.46	0.03

* This volume fraction corresponds to the *sc* structure.

ATOMIC FORCE MICROSCOPY (AFM)

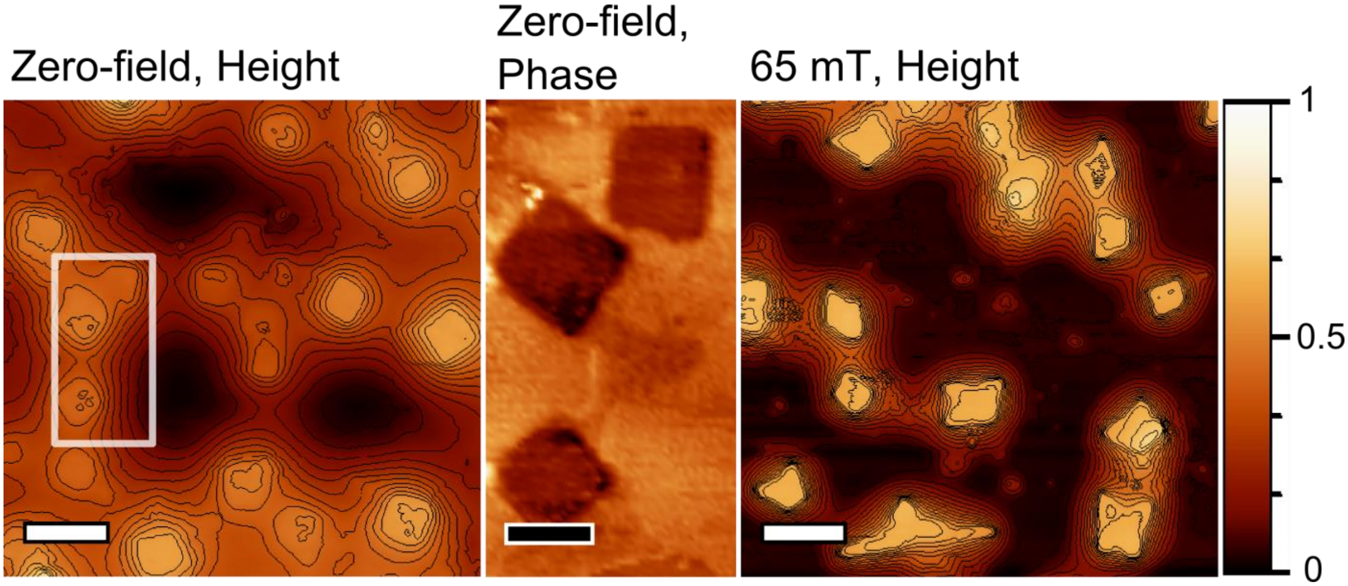

Figure S 10: AFM tapping-mode image of mesocrystals. Mesocrystals assembled in zero-field and in a magnetic field of $\mu_0 H_{app}$ = 65 mT. The middle image is the tapping mode phase image of the white area. which gives a significant contrast between the mesocrystals and the surrounding surfactant film. Scale bars. white: 5 µm. black 2 µm.

Phase and topography images of mesocrystals on Si-substrates were collected using a Veeco Bioscope-II AFM (Scanner size: 160 µm) operating in tapping-mode. A soft cantilever from *µ*masch with a nominal force constant of 3.5 N/m was used for all imaging (NSC18/AIBS. tip radius < 10 nm. f_r = 75 kHz). The images were processed using the WSxM software package (v. 5.0). [4]

SCANNING ELECTRON MICROSCOPY (SEM)

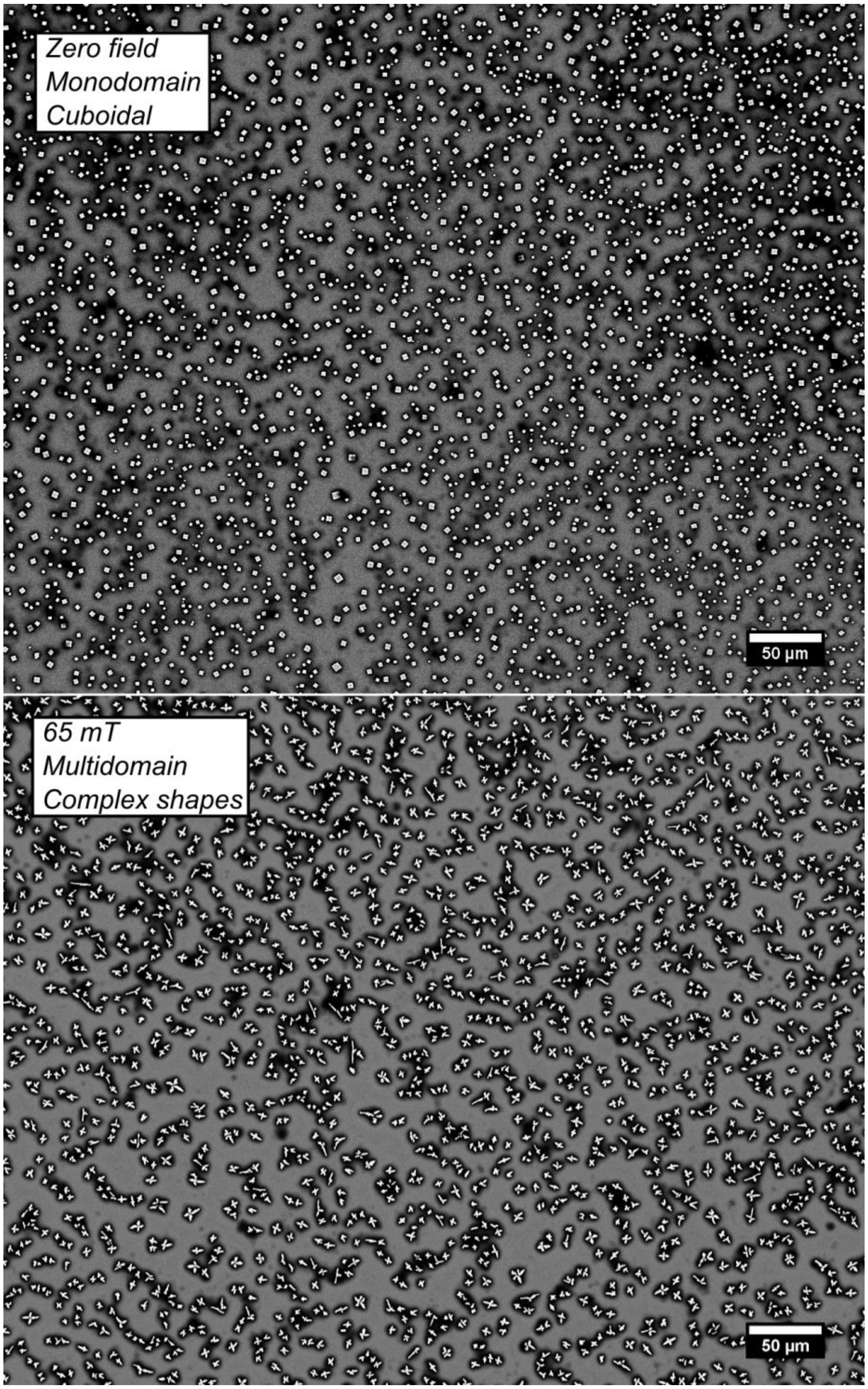

Figure S 11: Low magnification SEM images showing the large differences in the crystal morphologies. Images of the C096 mesocrystal sample assembled in: zero-field (top) and under magnetic field of $\mu_0 H_{app}$ = 65 mT (bottom).

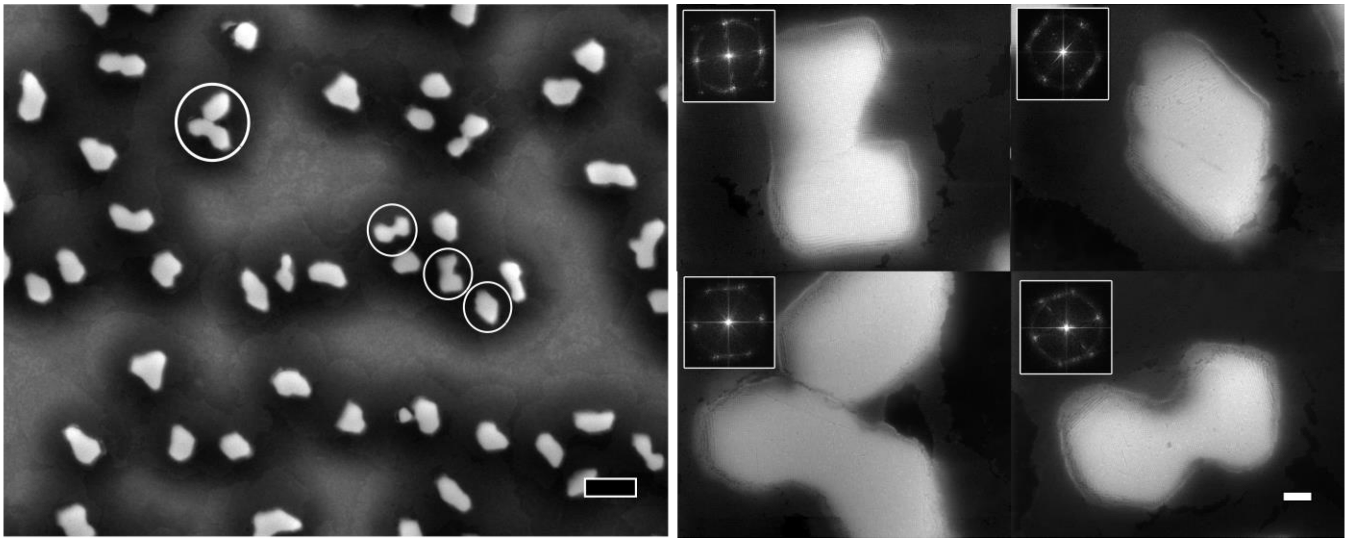

Figure S 12: Overview and HRSEM images of the C126 nanocube array assembled in a field of 65 mT. The complex mesocrystals have domains composed of both $[001]_{MC}$ and $[101]_{MC}$ oriented mesocrystal fragments. The insets show the fast Fourier transform of the mesocrystal surface. Scale bar: 1 µm (black). 200 nm (white). The three high resolution images have the same magnification.

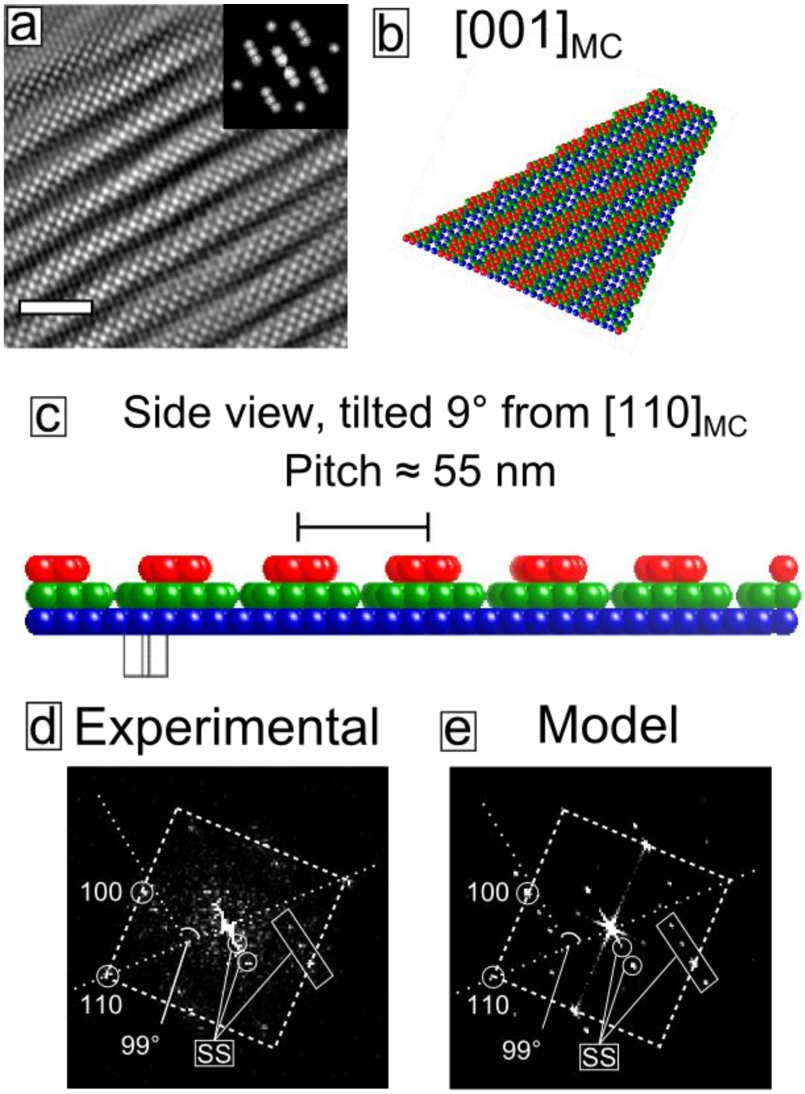

Figure S 13: Structural analysis of the periodic superstructure in a crystal fragment of an in-field assembled mesocrystal composed of 9.6 nm nanocubes. FFT-filtered portion of a domain in the mesocrystal in Figure 5a (*cf.* orange area). Inset: the corresponding FFT image. (b) Top view of a model of the corrugated surface seen in (a), viewed from the [100]$_{\text{MC}}$-zone axis of the *bct* mesocrystal. (c) Side view of the surface model. The "staircase"-undulations are cut at an angle of 9° with respect to the [110]$_{\text{MC}}$-zone axis of the *bct* mesocrystal. (d) FFT of an image of the mesocrystal surface in (a) and (e) FTT of an image of the proposed structure model. The indexing assumes a simple square unit cell (*p4m*). Some of the superstructure reflections are indicated by SS in the FFT patterns. The angle between the superstructure reflection series (marked by a rectangle) and the *p4m* base lattices is highlighted in the images.

Image reconstruction of wavy mesocrystal surface structures

In many elongated crystals (such as the crystal in Figure 4a and the orange fragment in Figure 5a) superstructure reflections appear in the FFT patterns which reduce the planar group symmetry from *e.g. p4mm* to *p2* symmetry. These reflections arise due to periodic surface undulations at the mesocrystals top surface, with one example clearly visible in the inset of Figure 4a. Here we performed a reconstruction of the mesocrystal surface using SEM images and compared it to a surface model. Figure S13 a shows the FFT filtered image of the mesocrystal surface (*orange area*, Figure 5a) displaying regular undulations, and its corresponding FFT. From the FFT pattern, it is possible to notice a number of superstructure reflections (marked SS) around the central spot, and along rods rotated by an angle of ≈ 99° relative to the $\boldsymbol{g}_{110}$ (*sc*) vector. These reflections are well-resolved, and spaced at a distance of $d^{-1} \approx 0.018(1)\ \mathrm{nm}^{-1} \rightarrow d = 56(3)$ nm. The measured pitch of the resulting surface undulations coincides with the distance $3\sqrt{2}a =$57.3 nm, suggesting a channel width of $3 \cdot d_{110}$. Hence a smooth, wavy interface with a matching pitch can be constructed by removing particles in the first and second layers of a *bct lattice* projected ≈ 9° away from the $[110]_{\mathrm{MC}}$-zone axis, as shown Figure S13b, c. The resulting FFT of the synthetic image is shown in Figure S13e, and essentially reproduces every feature of the FFT of the experimental SEM image.

Details of the image reconstruction

A surface model of the undulations observed in the mesocrystal *bct lattice* was generated using the Crystalmaker software suite. For comparison with the experimental structure, the surface model was projected from the [001]-zone axis and converted to a black-and-white image. To limit the image resolution and reproduce the SEM imaging conditions, the image was processed by applying a lens blur and a salt-and-pepper noise filter.

MAGNETOMETRY

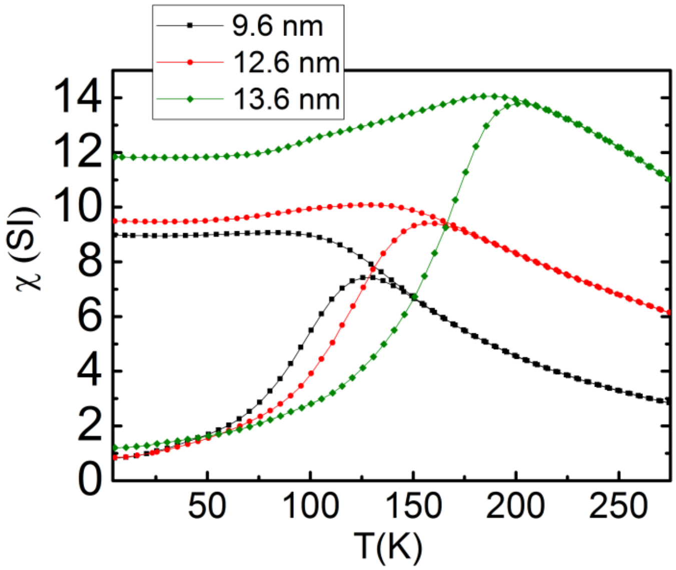

Figure S 14: **Zero-field cooled/field cooled (ZFC/FC) magnetization curves of nanocube mesocrystals assembled in zero-field.**

The measurement was performed in a Quantum Design SQUID MPMS XL. First, the sample was cooled to 5 K in zero-field. A magnetic field of 0.8 kA/m was applied parallel to the substrate. The moment of the sample is measured upon heating to 275 K (ZFC), and cooling back to 5 K (FC). The dimensionless magnetic susceptibility χ(SI) was calculated by determining the saturation moment of the sample, and normalizing it to a nanocube paste sample with a known mass of iron oxide particles. The density (ρ) of bulk Fe_3O_4 was used for the conversion of units. A ZFC/FC curve of the C086 nanocubes can be found in Ref [2]. Although there are different conventions, we have here simply approximated T_B with the cusp temperature of the ZFC curve.

References:

1 E. Wetterskog, M. Agthe, A. Mayence, J. Grins, D. Wang, S. Rana, A. Ahniyaz, G. Salazar-Alvarez and L. Bergström, *Sci. Technol. Adv. Mater.*, 2014, **15**, 055010.

2 S. Disch, E. Wetterskog, R. P. Hermann, G. Salazar-Alvarez, P. Busch, T. Brückel, L. Bergström and S. Kamali, *Nano Lett.*, 2011, **11**, 1651–1656.

3 K. Bian, J. J. Choi, A. Kaushik, P. Clancy, D.-M. Smilgies and T. Hanrath, *ACS Nano*, 2011, **5**, 2815–2823.

4 I. Horcas, R. Fernández, J. M. Gómez-Rodríguez, J. Colchero, J. Gómez-Herrero and A. M. Baro, *Rev. Sci. Instrum.*, 2007, **78**, 013705.